



Estimating volume of large slow-moving deep-seated landslides in northern Canada from DInSAR-derived 2D and constrained 3D deformation rates



Sergey V. Samsonov ^{a,*}, Andrée Blais-Stevens ^b

^a Canada Centre for Mapping and Earth Observation, Natural Resources Canada, 580 Booth St, Ottawa K1A0E4, Ontario, Canada

^b Geological Survey of Canada, Natural Resources Canada, 601 Booth St, Ottawa K1A0E8, Ontario, Canada

ARTICLE INFO

Editor: Jing M. Chen

Keywords:

Slow-moving deep-seated landslides
Surface-Parallel Flow (SPF)
Aspect-Parallel Flow (APF)
Landslide volume
Differential Interferometric Synthetic Aperture Radar (DInSAR)
Multidimensional Small Baseline Subset (MSBAS)
Canada
Alberta
Northwest Territories

ABSTRACT

Large slow-moving deep-seated landslides are observed in two different regions of northern Canada with advanced Differential Synthetic Aperture Radar (DInSAR). Two-dimensional vertical and horizontal east-west deformation rates and time series are computed from ascending and descending Sentinel-1 imagery acquired during 2017–2022. The landslides' east-west deformation rate is significantly larger than the vertical deformation rate, so it is better suited for landslide characterization. The deformation rates remain nearly constant and unaffected by seasonal changes during the entire period, suggesting substantial landslide thickness. Two large landslides in Alberta and the largest landslide in the Northwest Territories are studied in detail to demonstrate various advanced value-added products produced from DInSAR results. From ascending and descending line-of-sight deformation rates, Surface-Parallel Flow (SPF) and Aspect-Parallel Flow (APF)-constrained three-dimensional (3D) deformation rates are computed. Landslides thicknesses are then estimated from the APF-constrained 3D deformation rates, and the limitations of these techniques are discussed. The estimated thickness of the Northwest Territories landslide reaches 100 m, suggesting that the entire permafrost block may be sliding above the non-permafrost ground. The described techniques allow for mapping slow-moving deep-seated landslides in harsh conditions in areas affected by seasonal land cover changes, as in northern Canada. The decomposition of landslide motion into two or three components in certain conditions allows us to derive landslide thickness and volume and improve the estimation of a potential hazard posed by landslides.

1. Introduction

Landslides are natural hazards that pose a significant risk to population and infrastructure. Some landslides may not present detectable warning signals before failure; many, however, experience transient deformation, sufficient enough to be observed on the ground with ground or remote sensing measurement techniques (e.g., Dille et al., 2022). The Differential Interferometric Synthetic Aperture Radar (DInSAR) remote sensing technique (Massonnet and Feigl, 1998) is especially suitable for mapping mm- to cm-scale ground deformation produced by slow-moving deep-seated landslides over large areas and with high spatial resolution (Liu et al., 2013; Strozzi et al., 2018; Samsonov and Blais-Stevens, 2023; Li et al., 2023). Recent manifold increase in the availability of Synthetic Aperture Radar (SAR) data on a global scale from the European C-band Sentinel-1 constellation and the availability of low-cost processing resources encourage the use of DInSAR for landslide detection and monitoring at regional to global scales (Raspini

et al., 2018; Samsonov and Feng, 2023; Casagli et al., 2023). Novel advanced DInSAR processing techniques can characterize landslides in greater detail (Samsonov et al., 2020; Hu et al., 2020; Zheng et al., 2023); however, the limitations and advantages of these techniques are not yet well understood (DeLuca et al., 2017; Samsonov and Feng, 2023). In this study, we use advanced processing techniques (Samsonov et al., 2020; Hu et al., 2020) and report on their suitability for detecting and monitoring slow-moving deep-seated landslides and estimating their volume using the two sites in northern Canada as testing grounds.

The ultimate objective for using DInSAR is to measure with high temporal and spatial resolutions and with high precision the three (i.e., north-south, east-west, and vertical) deformation components (Hu et al., 2014; Shi et al., 2018; Hu et al., 2020; Samsonov et al., 2020; Zheng et al., 2023). This objective has not yet been achieved for several reasons described below.

The quality of individual DInSAR interferograms is usually low due to the temporal decorrelation and atmospheric noise. A loss of

* Corresponding author.

E-mail address: sergey.samsonov@nrcan-rncan.gc.ca (S.V. Samsonov).

interferometric coherence can be modelled as a product of several terms, with the two most significant terms proportional to the lengths of spatial and temporal baselines (Zebker and Villasenor, 1992). Modern space-borne SAR systems, specifically Sentinel-1, acquire data with small spatial baselines; it is, however, impractical on a global scale to reduce the temporal baseline beyond the current 6–12 days only for improving interferometric coherence. Thus, a loss of interferometric coherence due to temporal decorrelation will remain unresolved for the foreseeable future. Time series analysis techniques (Osmanoglu et al., 2016) derived from the Small Baseline Subset (SBAS) method (Berardino et al., 2002) use interferograms acquired with small spatial and temporal baselines to reconstruct deformation over an extended period. Recent systematic analyses of DInSAR data over Canada demonstrated that, in addition to temporal decorrelation, DInSAR is affected by noise due to seasonal penetration depth and snow water equivalent variability, which is particularly significant in regions with high topographic relief, where landslides typically occur (Samsonov and Feng, 2023), and also due to non-zero phase closures affecting multi-reference stacks of interferograms with exclusively short time intervals (Wegmüller et al., 2021).

DInSAR products capture ground deformation in the satellite line-of-sight (LOS) direction. By using ascending and descending DInSAR products, it is possible to reconstruct two (i.e. east-west and vertical) deformation components (Hu et al., 2014; Fuhrmann and Garthwaite, 2019). This technique is only accurate when the north-south deformation component is small, which a priori is unknown. Furthermore, it is possible to constrain the deformation and reconstruct three (i.e. north-south, east-west, and vertical) deformation components (Joughin et al., 1998; Hu et al., 2018). However, finding precise constraints without a priori knowledge is complicated at best. It is only in particular circumstances that it is possible to reconstruct all three deformation components, such as in the high Arctic (Gray, 2011), or if the extent of a landslide is large and the sliding rate is fast so that speckle offset tracking (Strozzi et al., 2002) or multiple aperture interferometry (Bechor and Zebker, 2006) techniques can be used. Even though the advanced component-decomposition methods compute only approximate solutions, they can provide valuable information for landslide characterization if we remain cautious of their limitations.

Northern Canada is a vast territory and an excellent candidate for applying remote sensing methods for detecting and monitoring landslides. Recent systematic analysis of DInSAR over Canada revealed several previously known and unknown areas with the largest, slow-moving deep-seated landslides in Canada (Samsonov and Feng, 2023). Here, we compute from DInSAR measurements various derived products and use them for studying these large landslides in detail. The methods presented here are tested in two areas to show their versatility.

2. Physiographic setting

The first study site in northern Alberta covers roughly 60,000 km² area over the Cariboo Mountains, located east of Highway 35, north of Fort Vermillion and Fox Lake, west of Lake Athabasca, and it touches the Northwest Territories border, southwest of Fort Smith. It also includes the western portion of Wood Buffalo National Park, Canada's largest national park.

The Cariboo Mountains form a plateau within the Northern Alberta Boreal Subarctic and Boreal Highlands, which is in Canada's Interior Plains. The areas that show slope deformation are located along the edge of the Cariboo Mountains plateau, where slope gradients are steepest.

The two main physiographic elements are the gently rolling highlands like the Cariboo Mountains separated by north or east-trending broad valleys (Fenton et al., 2003). The highest elevation in this area is 1100 m asl, and the lowest is 70 m asl.

The bedrock is mainly Cretaceous in age with some younger Paleogene sediments (Tertiary gravels) overlying horizontally bedded shales and sandstones from the Smoky Group, Dunvegan, Shaftesbury, and Peace River formations reflecting deltaic and marine environments

(Green et al., 1970).

Surface sediments over the Cariboo Mountains deposited mainly during the last glaciation and subsequent deglaciation vary between 15 and 45 m in thickness (Fenton et al., 2003). Sediments from the Pleistocene are composed of till, glaciofluvial, and glaciolacustrine deposits. Those from the Holocene consist of fluvial, lacustrine, eolian, and colluvial deposits with very few bedrock exposures. Some slopes show creep deformation due to the presence of permafrost (Mougeot and Fenton, 2010) as the study area falls within sporadic discontinuous permafrost (Heginbottom et al., 1995).

Present-day climate conditions are marked by cool summers and cold winters. The mean annual temperature ranges from -2 °C to -2.5 °C. The mean summer temperature ranges from 13 °C to 14 °C, and the mean winter temperature from -18 °C to -20 °C. The mean annual precipitation ranges from 350 to 500 mm.

A landslide susceptibility study for the Interior Plains and Canadian Shield regions published by Pawley et al. (2016) indicates that the area around the edge of the Cariboo Mountains, where the slope gradient is steep, reflects terrain with high landslide susceptibility.

The second study site in the Northwest Territories covers roughly 1,100 km² within the Richardson Mountains. Its western limit is situated just east of the Yukon border, and its eastern limit is located at the edge of the Mackenzie River Delta alluvial plain. The northeast corner of the study area is roughly 25 km southwest of Aklavik, and the southeast corner is roughly 45 km north-northwest of Fort Simpson. It is located within mostly continuous permafrost (Heginbottom et al., 1995). Relief in the mountains consists of rounded ridges and wide valleys. The highest elevation point is 1000 m in the mountains, and the lowest is 5 m on the delta (Duk-Rodkin, 1992).

Surficial geology sediments are the result of Pleistocene glaciations reflected in the presence of glacial and deglacial deposits (Duk-Rodkin and Hughes, 1994). Glacial sediments consist of till and deglacial sediments, gravels, sands, silts, and clays. Some of the higher bedrock elevation points were not glaciated during the last glaciation (Duk-Rodkin and Hughes, 1994).

The bedrock in this study area consists of sedimentary rock formations that are mainly marine in origin. They vary from Permian to Cretaceous in age and are composed mainly of shales, siltstones, sandstones, and quartzose. The sediments belong to, from youngest to oldest, the Parsons Group, Mount Goodenough Formation, Husky Formation, Bug Creek Group, and an undifferentiated Permian marine fine-grained unit. Regional bedrock structure reveals large amplitude, linear to curvilinear folds (Lane and Dietrich, 1996).

The climate is defined by long very cold winters and short summers. Temperature values range from -27 °C in the winter (January 2006) to 27 °C in the summer (July 2006). Total yearly precipitation is around 300 mm, which is considered a dry climate (Aklavik climate station; Environment Canada, 2023).

The prominent types of landslides in this study area are ones originating from weathered bedrock as colluvium and some retrogressive thaw slump in permafrost-rich fine-grained sediments (Duk-Rodkin, 1992; Aylsworth et al., 2000).

3. Data and methodology

We processed six sets of Sentinel-1 Synthetic Aperture Radar (SAR) images in Single Look Complex (SLC) format acquired over two regions in northern Canada during 2017–2022 (Fig. 1). In Alberta, we used two ascending sets from tracks 020 and 049 and one descending set, consisting of two concatenated frames, from track 042. In the Northwest Territories, we used two ascending sets from tracks 079 and 108 and one descending set from track 116. To reduce the amount of the required processing in the Northwest Territories, we took only two bursts of a single subswath per set. For example, from track 079, we took bursts 1 and 2 of subswath 3. Detailed data information is provided in Tables 1

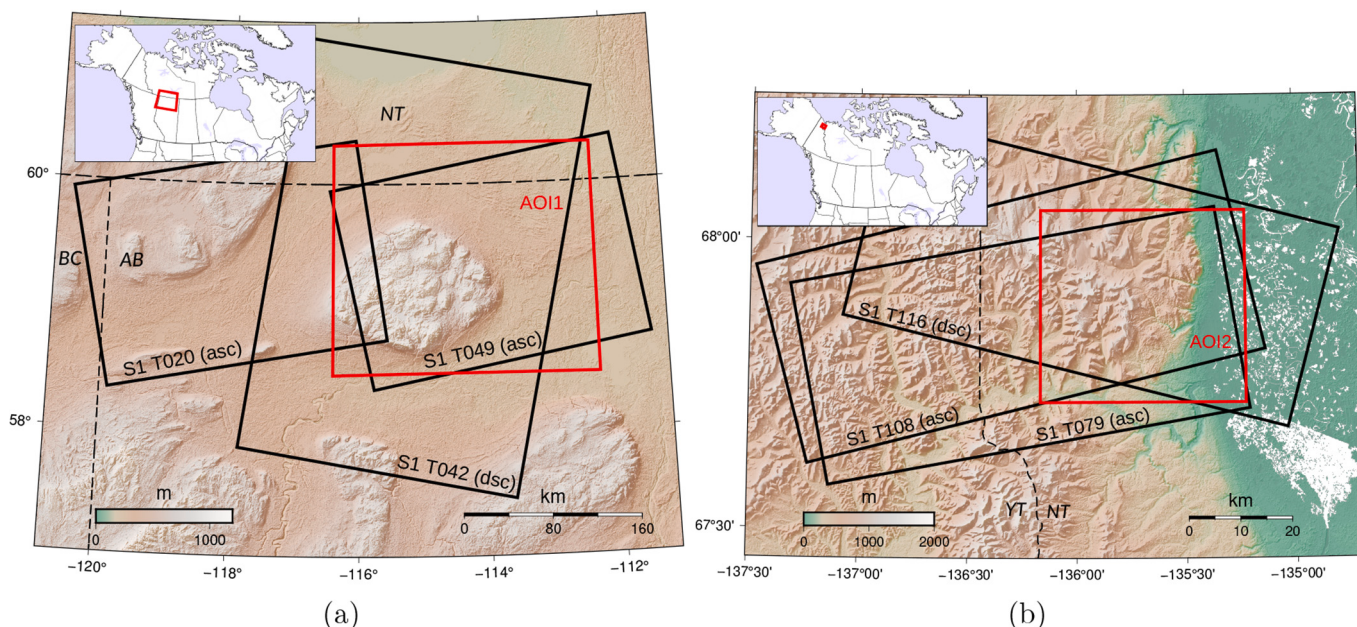


Fig. 1. Two areas of interest (AOI) located in northern Canada are outlined in red: (a) AOI1 in Alberta and (b) AOI2 in Northwest Territories. Ascending and descending Sentinel-1 swaths are outlined in black. Provincial boundaries are shown as dashed black lines. Background in (a) is 30 m Advanced Spaceborne Thermal Emission and Reflection Radiometer (ASTER) DEM and (b) is 2 m resolution ArcticDEM. AB-Alberta, BC-British Columbia, NT-Northwest Territories, YT-Yukon. Insets in top-left corners show location of these regions in North America. (For interpretation of the references to colour in this figure legend, the reader is referred to the web version of this article.)

and 2.

Each Sentinel-1 set was processed independently with the GAMMA software (Wegmüller and Werner, 1997) on a High-Performance Computer (HPC) Linux cluster operated by the Canadian Government (Dudley and Samsonov, 2020). The fully automated processing strategy in detail is described in Samsonov and Feng (2023) and is summarized below. Three interferograms with the shortest temporal baselines of 12, 24, and 36 days were computed for each primary image, and highly coherent interferograms were retained for the time series analysis. The MSBAS version 10 software was used for calculating the two-dimensional (2D) deformation rates and time series for each pixel. This technique is further referred to as MSBAS-2D. For the study site in northern Alberta, we performed two MSBAS-2D runs each time using one of two available ascending and same descending sets, which allowed us to increase spatial coverage. For the study site in the Northwest Territories, we simultaneously processed one descending and two ascending sets, achieving, in comparison to the runs for the Alberta site, about 1.5 times denser temporal resolution (Tables 1–2).

The MSBAS version 10 software is a recent version (Samsonov and Oreye, 2012) designed to run on multiple nodes of an HPC. This modification improves the processing time by a factor equal to the number of

Table 1

Sentinel-1 SAR data (track and frame) used in Alberta, where θ is azimuth and ϕ is incidence angles, nSLC and nInSAR are numbers of available images and interferograms produced.

Data	Span	θ^*	ϕ^*	nSLC	nInSAR
T020 F191 (asc)	01 Mar. 2017 – 12 Dec. 2021	342	39	119	207
T049 F191 (asc)	27 Mar. 2017 – 12 Dec. 2021	342	39	120	211
T042 F391/397 (dsc)	27 Mar. 2017 – 12 Dec. 2021	198	39	140	229
Total: T020-T042	01 Mar. 2017 – 12 Dec. 2021			259	439
Total: T049-T042	27 Mar. 2017 – 12 Dec. 2021			258	440

Table 2

Sentinel-1 SAR data (track, frame, subswath-bursts) used in Northwest Territories, where θ is azimuth and ϕ is incidence angles, nSLC and nInSAR are numbers of available images and interferograms produced.

Data	Span	θ^*	ϕ^*	nSLC	nInSAR
T079 F221 IW3-1,2 (asc)	20 Oct. 2016 – 07 Oct. 2022	338	43	147	246
T108 F221 IW1-4,5 (asc)	19 Mar. 2017 – 29 Mar. 2022	338	33	128	262
T116 F366 IW1-3,4 (dsc)	20 Oct. 2016 – 07 Oct. 2022	202	33	164	262
Total:	20 Oct. 2016 – 07 Oct. 2022			437	770

nodes. In our processing, we typically use ten nodes that contain 40 cores each, so the processing time is reduced by a factor of ten, from approximately ten days to one day per MSBAS run. The MSBAS software no longer requires the pixels to be coherent in every interferogram while preserving the temporal resolution and coverage of many pixels. The processing quality at each pixel depends on the rank of the matrix that comprises the inverse problem. The low-quality pixels can be identified and removed by analyzing matrix rank values after the MSBAS run (Samsonov and Feng, 2023).

From the MSBAS's output in GeoTiff format, we extracted for selected twenty 5×5 -pixel fast-moving regions 2D deformation time series with corresponding confidence intervals plotted as error bars. The error bars, however, do not capture systematic errors for the entire 5×5 pixel region. We also extracted cumulative deformation time series along various profiles and plotted them as images; this is a similar approach to the one describing the temporal evolution of flow velocities of glaciers (e.g. Samsonov et al., 2021).

The 2017–2022 ascending and descending LOS deformation rates were also computed with MSBAS. This technique is further referred to as MSBAS-1D. Then ascending and descending LOS rates were used to calculate three-dimensional (3D) deformation rates assuming a Surface-Parallel Flow (SPF) (Joughin et al., 1998; Samsonov et al., 2020) and

Aspect-Parallel Flow (APF) (Hu et al., 2018) constraints over two regions that cover three large landslides; two in Alberta and one in the Northwest Territories. These techniques are further referred to as MSBAS-3DSPF and MSBAS-3DAPF. The 3DSPF methodology has been previously used for computing 3D flow velocities from DInSAR data of slow-moving glaciers and 3D deformation rates of a large slow-moving deep-seated landslide in the Democratic Republic of the Congo (Samsonov et al., 2020; Dille et al., 2022). The SPF constraint assumes that the sliding happens along a plane parallel to a smoothed ground surface. The 3DAPF constraint assumes that the sliding happens along the vertical plane parallel to the slope aspect (Hu et al., 2018). The surface topography, derived from the DEM, is spatially low-pass filtered to remove fine-scale surficial features (e.g., large boulders, ridges) while preserving the overall trend and is used to compute directional topographic derivatives in the north and east directions and slope aspect. In this study, spatial low-pass filtering is performed using the Gaussian window with a six-sigma radius of 0.6 km.

Based on a sensitivity analysis performed using the actual time matrix from the Northwest Territories region, we aimed to understand the impact of inaccurate estimation of topographic gradients and slope aspect angle. It was found that the error in the DEM-derived parameters could stem from the sliding plane's geometry differing from the surface topography and filtering-induced artifacts. The configuration used for this analysis assumed that the actual topographic gradients in the east and north directions are -0.5 m/m and that the slope aspect is 45 degrees, which corresponds to sliding precisely in the northeast direction, with north, east, and vertical rates of 0.1, 0.1, and -0.1 m/year, respectively. By deviating the values of estimated topographic gradients and slope aspect in the range -1.0 to 0 m/m and from 0 to 90 degrees, respectively, we recorded and plotted the estimated deformation rates in Fig. 2. It was observed that the error propagation is nearly linear for small values of error in the DEM-derived parameters. However, for large errors in the DEM-derived parameters, the error in the estimated north and vertical deformation rates is also large, while the east component is estimated relatively accurately. The landslides studied in detail below slide predominantly along east-west directions.

For the two largest landslides in Alberta and the largest landslide in the Northwest Territories, we compute the landslides' thickness using

3DAPF deformation rates and a methodology outlined by Booth et al. (2013); Hu et al. (2018). The law of mass conservation, under the assumption of incompressibility, requires the 3D deformation field to be divergence-free ($\nabla \cdot V = 0$) or

$$\frac{\partial h}{\partial t} = -\nabla(h\bar{V}_{hor}), \quad (1)$$

where V is the 3D deformation rate vector, \bar{V}_{hor} is the depth-averaged 2D horizontal deformation rate vector, and h is the landslide thickness. Assuming that the basal height does not change over the observation time, the rate of thickness change $\frac{\partial h}{\partial t}$ is equal to the observed vertical deformation rate V_{vert} and the depth-averaged 2D horizontal deformation rate vector \bar{V}_{hor} is equal to the fV_{hor}

$$V_{vert} = -\nabla(hfV_{hor}), \quad (2)$$

where f is a coefficient that depends on the rheological properties of the moving mass, which ranges from 0 to 1. In this study, we assumed $f = 0.7$ (representative of approximately Newtonian viscous flow) for the landslides in Alberta and $f = 1.0$ (representative of a rigid sliding block with no yield zone) for the landslide in the Northwest Territories. A larger f value was chosen for the landslide in the Northwest Territories because it is located in the continuous permafrost zone. A regularization added to eq. (2) produces a smoothed version of the landslide thickness. The reasons for using 3DAPF deformation rates are discussed below.

To accurately apply eq. (2), we need to know vertical and horizontal velocities in the coordinate system parallel to the sliding surface. For this, we need to know the dip angle of the sliding surface at each pixel. Using the DEM-derived dip angle at the surface would be inaccurate for many landslides (e.g., rotational landslides). We, however, can assume that the sliding surface dip angle is constant. In that case, eq. (2) can be rewritten for vertical and horizontal velocities in the flat-earth references frame, observed with DInSAR. However, the assumption that the dip angle is constant implies that the landslide is translational. Thus, this approximation is only valid for translational landslides since it does not account for the variability in the sliding surface dip angle.

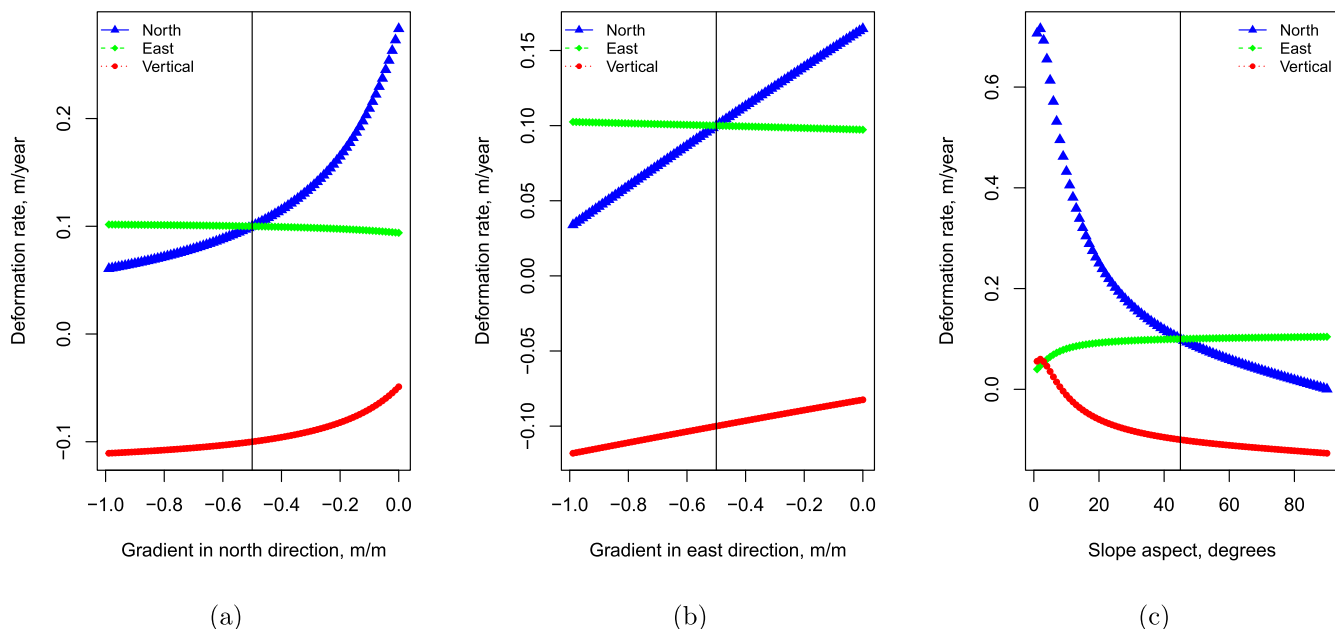


Fig. 2. Sensitivity analysis to errors in topographic gradients (3DSPF technique) and slope aspect (3DAPF technique). Correct parameters, marked with vertical lines, are -0.5 and -0.5 m/m north and east topographic gradients, 45 degrees slope aspect, 0.1, 0.1, and -0.1 m, deformation rate in north, east and vertical directions, respectively.

4. Results

The MSBAS-2D east and vertical deformation rates are shown in Fig. 3 for the two studied regions. These results were spatially high-pass filtered (using 256 pixels window) to remove the long wave-length signal unrelated to the landslide deformation. The histogram of deformation rates and their standard deviation are shown in the inserts; the values are in a range of 0.01–0.02 m/year, significantly lower than the deformation rates of the landslides.

Among several landslides visible in Fig. 3, we focused on the three largest landslides. Two of them (Landslide 1 to the left and Landslide 2 to the right) are located in Alberta in the area marked AOI1a in Figs. 3(a,b), and the third (Landslide 3) is located in the Northwest Territories in the area AOI2a in Figs. 3(c,d). We first show MSBAS-2D results because, while approximate (i.e., they do not account for deformation along the north-south direction), they do not depend on the choice and filtering strength of the DEM.

For several large landslides, the 2D deformation time series

computed with the MSBAS-2D technique are shown in Fig. 4. They were calculated for small, 5×5 -pixel regions centered on local deformation extrema. For consistency, the range of the Y-axis is set equal to 2 m in Fig. 4(a-s) and 3 m in Fig. 4(t). The deformation rate is nearly constant in most regions except for sites P12 and P15, where a moderate increase in the deformation rate was observed in 2020. At all these sites, except for P16, horizontal deformation rates exceed vertical deformation rates, which is expected for landslides along gently dipping slopes. At site P16, the horizontal and vertical deformation rates are approximately equal.

The MSBAS-2D results for two landslides in Alberta are shown in Fig. 5. The isolines of the east-west deformation rate plotted over the best available for this region 30 m resolution DEM is shown in Fig. 5(a). The deformation rate ranges from 0.08 (orange) to 0.26 (purple) m/year. Solid lines represent eastward deformation and dashed lines westward deformation. The magnitude of the cumulative east-west deformation time series extracted along profiles A1B1, C1D1, A2B2, and C2D2 are shown in Figs. 5(b-e).

The MSBAS-2D results for a landslide in the Northwest Territories are

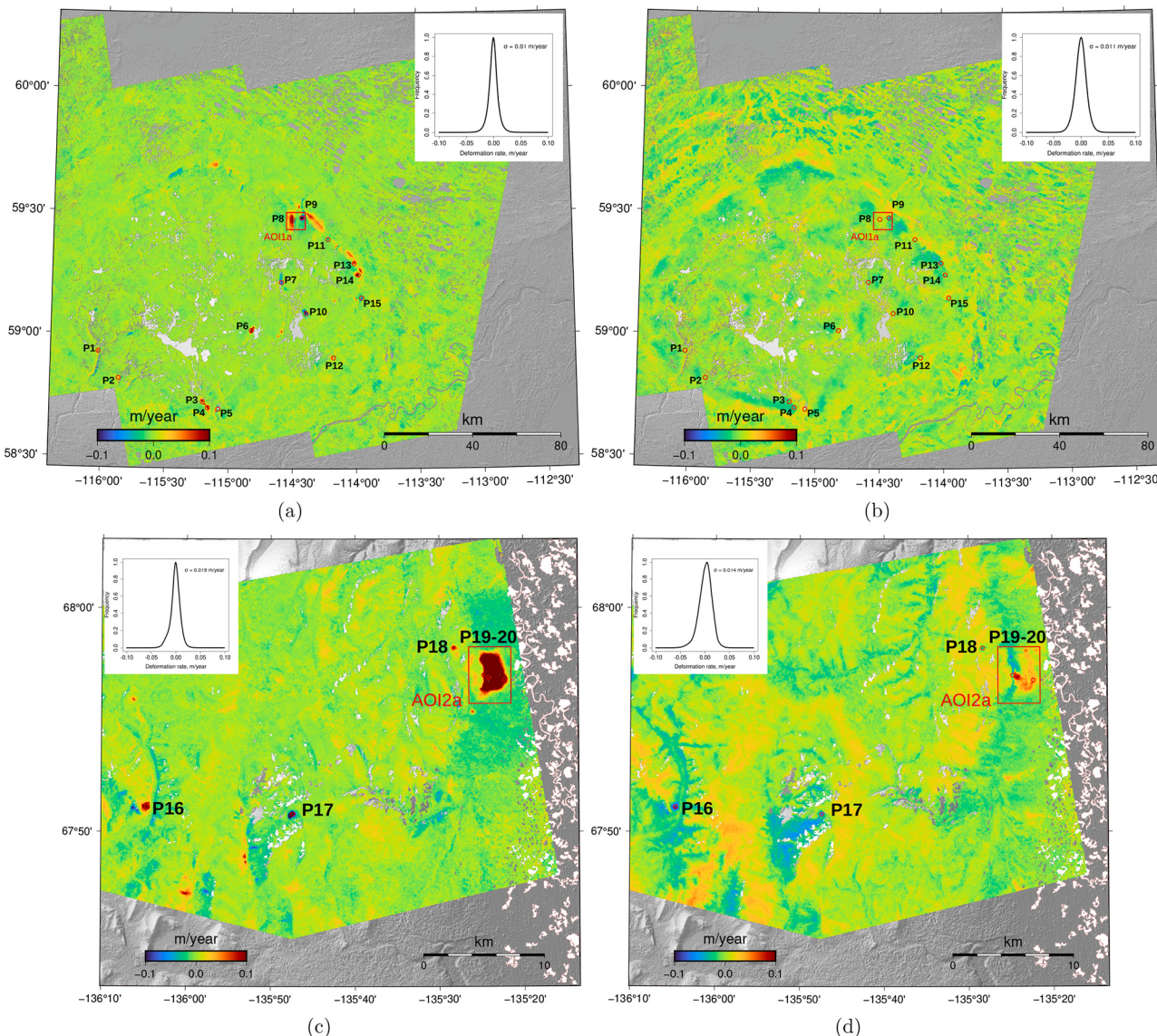


Fig. 3. East-west (a,c) and vertical (b,d) deformation rates from MSBAS-2D decomposition in Alberta (top row) and Northwest Territories (bottom row) during 2017–2022, computed from ascending and descending Sentinel-1 data. Colour scales are clipped to ± 0.1 m/year. Inserts show histograms of deformation rates and their standard deviation. Small areas of interest AOI1a in Alberta and AOI2a in Northwest Territories, outlined in red, are studied in more detail. For 5×5 regions P1–P20 two dimensional deformation time series are extracted and shown in Fig. 4. Background as in Fig. 1. (For interpretation of the references to colour in this figure legend, the reader is referred to the web version of this article.)

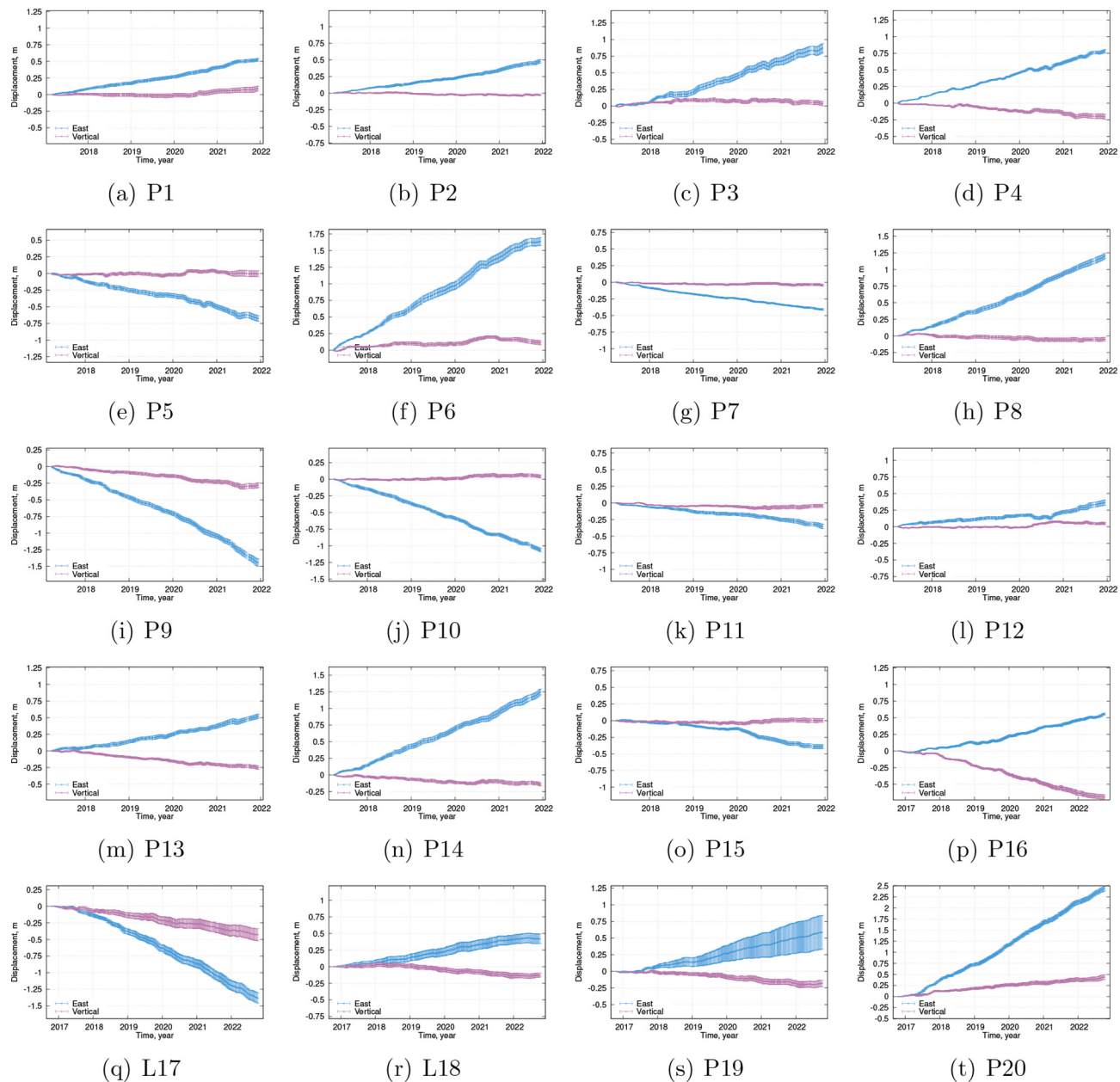


Fig. 4. Cumulative east-west and vertical deformation time series from MSBAS-2D decomposition during 2017–2022 for 5×5 pixel regions P1–P15 in Alberta and P16–P20 in Northwest Territories. Range of Y-axis equals 2 m in (a–s) and 3 m in (t). Note that in most regions horizontal deformation rate exceeds vertical deformation rate.

shown in Fig. 6. The isolines of the east-west deformation rate plotted over 2 m resolution DEM are shown in Fig. 6(a). The eastward deformation rate ranges from 0.10 (dark red) to 0.44 (purple) m/year. The high-resolution DEM in the background clearly shows remnants of the past surface deformation and the deposits (see inset surficial geology map in Fig. 6(a)) extending to the north beyond the area experiencing active deformation during 2017–2022. The magnitude of the cumulative east-west deformation time series extracted along profiles A3B3 and C3D3 are shown in Figs. 6(b, c) and the cumulative vertical deformation time series, extracted along these profiles are shown in Figs. 6(d, e). The deformation rate along the two profiles remains nearly constant during 2017–2022. Particularly interesting is that the vertical deformation rate in Figs. 6(d, e) abruptly changes from downward, which is interpreted as the zone of depletion, to upward in the zone of accumulation, at regions marked with red lines, and it seems that these transitioning regions creep towards the southeast.

Then 2017–2022 ascending and descending LOS deformation rates were computed with the MSBAS-1D technique and from these LOS deformation rates, two sets of the 3D (i.e., north, east, vertical) deformation rates were computed, assuming (i) SPF constraint with the MSBAS-3DSPF method and (ii) APF constraint with the MSBAS-3DAPF method. These techniques can be applied to the entire region, but it would also require computing regionally-smoothed north and east topographic gradients and the slope aspect. Instead, to reduce computational intensity, the extent of 3D deformation rates is limited to the landslide extent. The constrained 3D decomposition techniques can also be applied to the original interferograms as it was done during the 1D and 2D processing, thus, producing constrained 3D time series for each pixel, but it is beyond the scope of this study.

The MSBAS-3D results for two landslides in Alberta are shown in Fig. 7. The topographic gradients used for 3DSPF processing are shown in Figs. 7(a–b) and the slope aspect in Fig. 7(d). The 3DSPF deformation

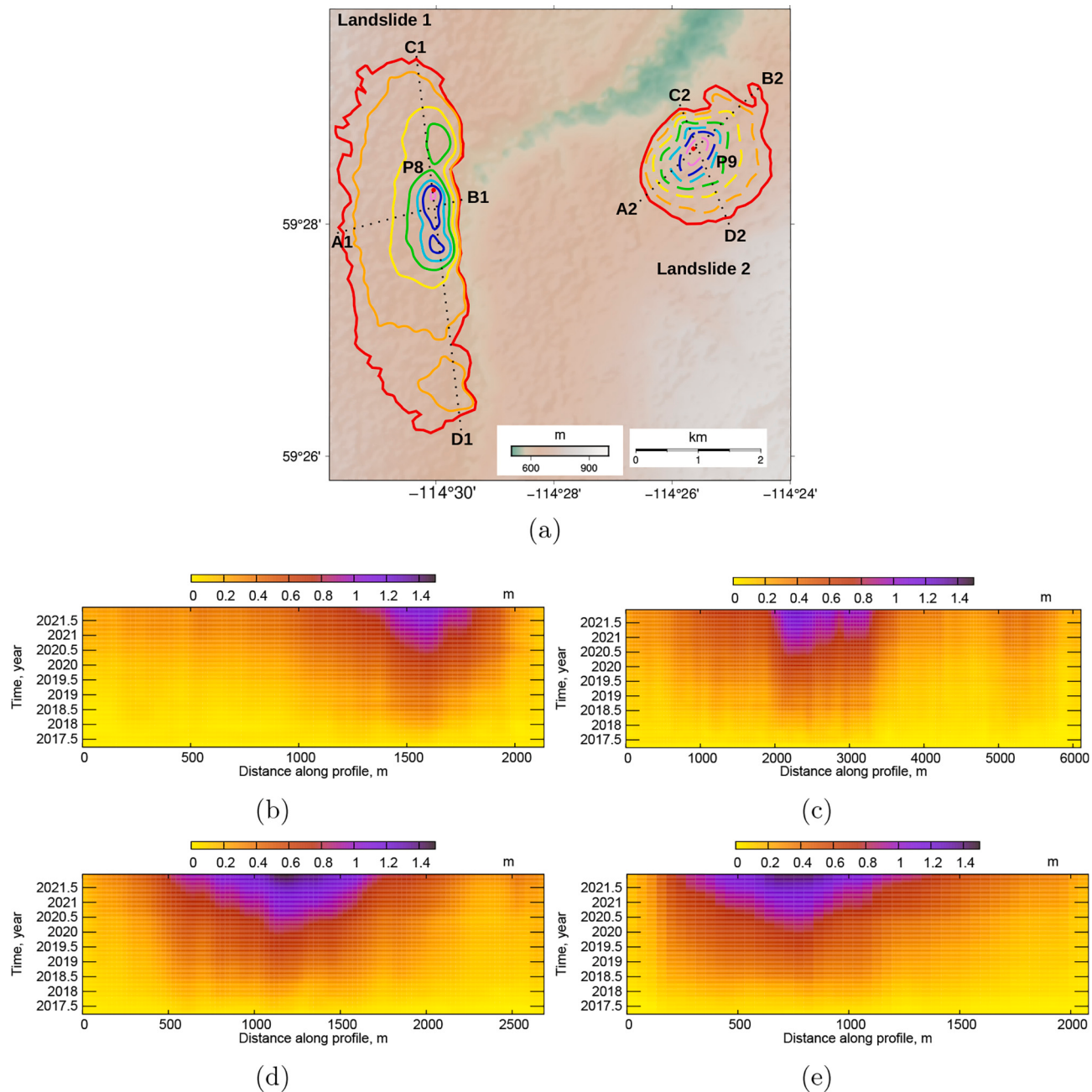


Fig. 5. Results of MSBAS-2D processing for Landslides 1 and 2. (a) Contour lines of east-west deformation rate in range 0.08 (orange) to 0.26 (purple) m/year (solid lines - eastward, dashed lines - westward). Red dots show locations of regions P8 and P9. (b-e) Magnitude of cumulative east-west deformation across profiles A1B1, C1D1, A2B2 and C2D2, respectively. Red lines outline landslide extent. Background is 30 m resolution ASTER DEM. (For interpretation of the references to colour in this figure legend, the reader is referred to the web version of this article.)

rates for two landslides are shown in Fig. 7(c) and the 3DAPF deformation rates in Fig. 7(e). Horizontal deformation is represented with vectors, and vertical deformation is colour-coded. The sliding direction of Landslide 1 (P8) is predominantly towards the east, while at Landslide 2 (P9), the direction is from southwest to northwest. The landslide thickness, computed with eq. (2) from results in Fig. 7(e), is shown in Fig. 7(f). The values range from 0 to 25 m (Landslide 1) and 0 to 55 m (Landslide 2).

The MSBAS-3D results for a landslide in the Northwest Territories are shown in Fig. 8. The topographic gradients used for 3DSPF processing are shown in Figs. 8(a-b) and the slope aspect in Fig. 8(d). The 3DSPF deformation rates for the landslide are shown in Fig. 8(c) and the 3DAPF deformation rates in Fig. 8(e). Horizontal deformation is represented

with vectors, and vertical deformation is colour-coded. The predominant sliding direction is eastward, but the north-south deformation is also present in different parts of this landslide. The landslide thickness, computed with eq. (2) from results in Fig. 8(e), is shown in Fig. 8(f). The values range from 0 to 100 m.

For comparing MSBAS-3DSPF and MSBAS-3DAPF solutions, a Root Mean Square Error (RMSE) of the differences was computed for the three studied landslides. For the landslide in the Northwest Territories, the north, east and vertical RMSEs were 0.085, 0.034, and 0.013 m/year. For Landslide 1 in Alberta, the north, east and vertical RMSEs were 0.023, 0.008, and 0.004 m/year; and for Landslide 2 in Alberta, the north, east and vertical RMSEs were 0.026, 0.015, and 0.005 m/year. The largest discrepancy is observed in the north component of the

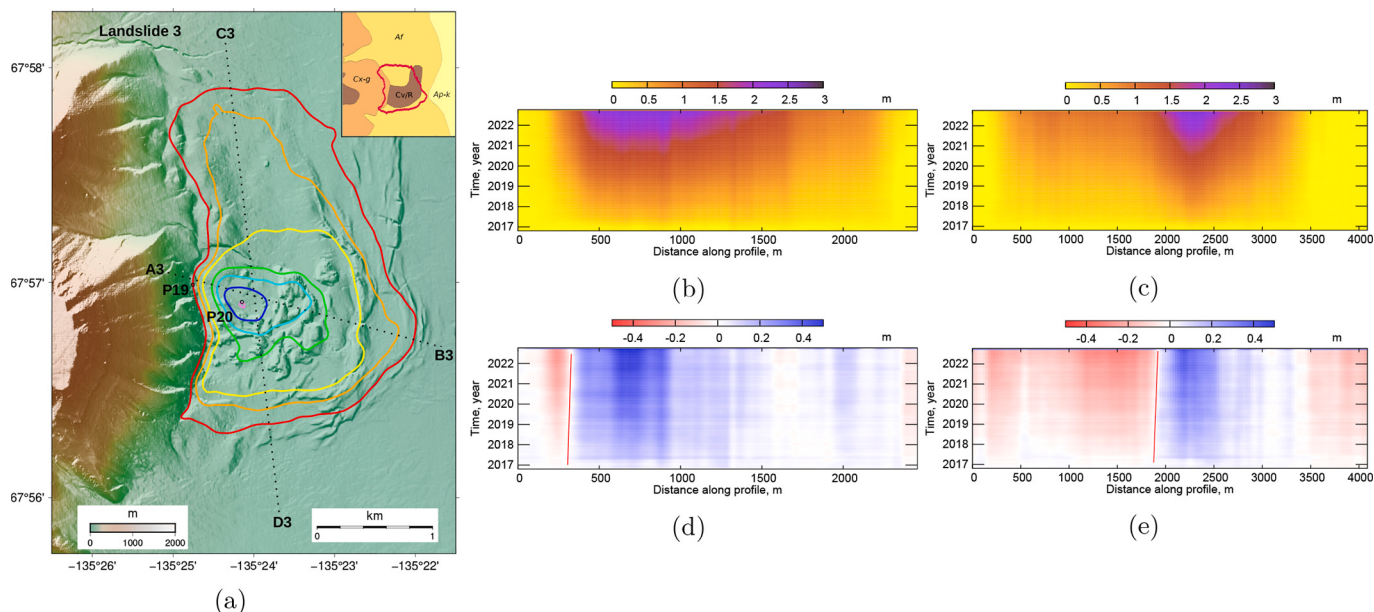


Fig. 6. Results of MSBAS-2D processing for Landslide 3. (a) Contour lines of east-west deformation rate in range 0.10 (dark red) to 0.44 (purple) m/year. Black dots show locations of regions P19 and P20. (b-c) Cumulative magnitude of east-west deformation across profiles A3B3 and C3D3, and (d-e) cumulative vertical deformation across profiles A3B3 and C3D3. Creep regions of abrupt change from downward to upward deformation marked with red lines. Inset in (a) is surficial geological map (modified from Duk-Rodkin (1992); Côté et al. (2013)). Af - alluvial deposits (fans and aprons), Ap-k - alluvial deposits (floodplain sediments containing thermokarst depressions), Cv/R - discontinuous veneer overlaying bedrock 0–2 m thick, Cx-g - slope complex (dominantly gravel). Background is 2 m resolution ArcticDEM. (For interpretation of the references to colour in this figure legend, the reader is referred to the web version of this article.)

landslide in the Northwest Territories caused by the variability in the surface topography in the centre of the landslide (Figs. 8(c-e)); even then, RMSEs are significantly lower than the observed deformation signal. As determined by the sensitivity analysis (Fig. 2), the RMSE of the north component is larger than the RMSE of the east and vertical components.

During 2017–2022, the deformation rate was nearly constant, but in the Northwest Territories especially, the presence of remnants of the past surface deformation suggests that, prior to 2017, the landslide extended beyond its current boundaries. However, in Duk-Rodkin (1992); Côté et al. (2013)'s surficial geology map, the area outlined was smaller (inset in Fig. 6(a)). This could be due to the fact that slow deformation in the form of creep was observed but displayed less of a footprint, or the area has since grown. It could also be due to the fact that the observations were made with coarse-resolution air photos vs. long-term high-resolution DInSAR surface deformation signals overlain on a high-resolution DEM. The volume of Landslides 1–3 are 0.12, 0.06, and 0.26 km³, computed assuming an estimated average thickness of 13, 18, and 42 m.

5. Discussion

Several processing techniques presented here can be used, under certain conditions, for landslide characterization.

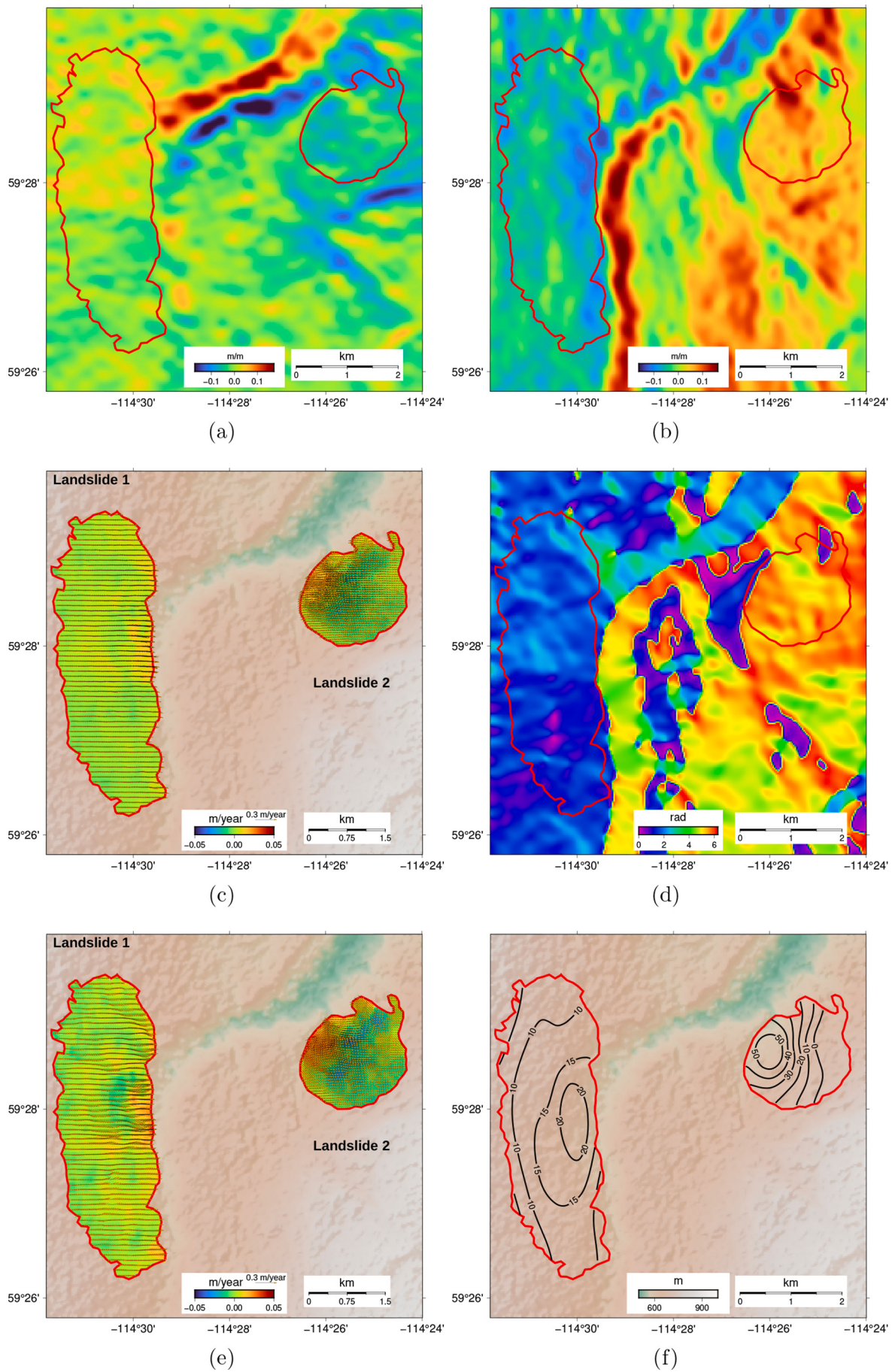
5.1. DInSAR and 1D time series

Fully automated processing systems nowadays are used for computing DInSAR interferograms, and subsequently, from computed interferograms, the LOS deformation time series and deformation rates can be generated using SBAS-derived techniques. It is expected that fully automated processing systems will replace manual processing entirely as the amount of SAR data increases. An operator of an automated processing system ultimately does not verify the quality of individual interferograms and only analyses deformation time series and, perhaps, the overall (i.e., mean) deformation rates. A fully automated processing

system decides which interferograms to select for the time series analysis based on a specified algorithm (e.g., Smittarello et al., 2022; Samsonov and Feng, 2023). Temporally-decorrelated areas in selected interferograms are removed, either before or after phase unwrapping, usually using coherence as a threshold. The smaller the coherence threshold value (ranging from zero to one), the better the resulting spatial coverage and the higher the probability of incorrect phase unwrapping. Temporal decorrelation is significant in regions with a rapid seasonal change in land cover vegetation conditions, such as northern Canada. Therefore, small threshold values of the coherence are selected to achieve good spatial coverage. This process, however, increases the probability of incorrect phase unwrapping and usually results in a loss of a part of the deformation signal. Deformation rates produced by fully automated processing systems, thus, are expected to be underestimated. It is possible to compute the deformation rate over a short period using SAR data acquired with a small repeat cycle (such as RCM with a 4-day repeat cycle) to improve measurement precision of the deformation rate; however, such SAR data are not yet readily available.

DInSAR interferograms measure a linear combination of three deformation components equal to the projection of the deformation vector on the satellite line-of-sight. Horizontal and vertical deformation components produced by a landslide can cancel each other out, partially or entirely, in a particular orbital geometry. For example, in interferograms from ascending orbits, downward and westward deformation cancel each other out, and in interferograms from descending orbits, it is the downward and eastward deformation that cancel each other out. The ascending and descending LOS deformation products cannot be easily cross-validated by an automated system, as they may look very different. Even an experienced researcher or operator can misclassify landslide-induced deformation as noise due to its presence only in ascending or descending LOS products. Below, we show that using 2D deformation products instead solves this issue.

When only interferograms acquired with short temporal baselines, such as 6–12 days in the case of Sentinel-1, are used for time series analysis, the resulting deformation time series may contain a systematic error due to spatio-temporal variability in SAR penetration depths



(caption on next page)

Fig. 7. Supplementary data and results of (a-c) MSBAS-3DSPF and (d-f) MSBAS-3DAPF processing for Landslides 1 and 2. Topographic gradients in (a) north and (b) east directions. (c) Horizontal (vectors) and vertical (colour-coded) deformation rates from 3DSPF decomposition. (d) Topographic aspect angle, measured from north clockwise. (e) Horizontal (vectors) and vertical (colour-coded) deformation rates from 3DAPF decomposition. (f) Contour lines of landslide thickness (in meters) derived from 3DAPF deformation rates. Red lines outline landslide extent. Background is 30 m resolution ASTER DEM. (For interpretation of the references to colour in this figure legend, the reader is referred to the web version of this article.)

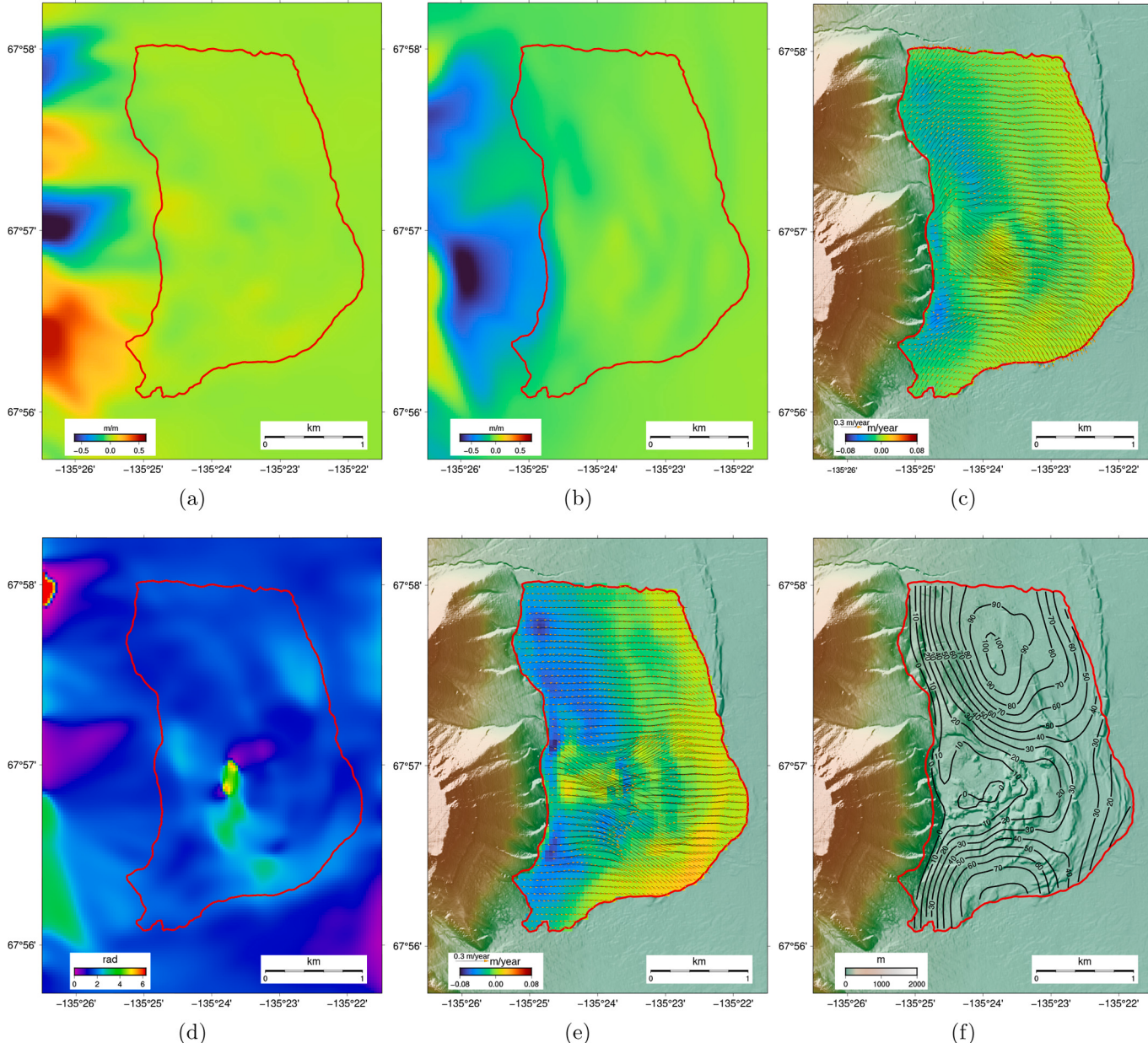


Fig. 8. Supplementary data and results of (a-c) MSBAS-3DSPF and (d-f) MSBAS-3DAPF processing for Landslide 3. Topographic gradients in (a) north and (b) east directions. (c) Horizontal (vectors) and vertical (colour-coded) deformation rates from 3DSPF decomposition. (d) Topographic aspect angle, measured from north clockwise. (e) Horizontal (vectors) and vertical (colour-coded) deformation rates from 3DAPF decomposition. (f) Contour lines of landslide thickness (in meters) derived from 3DAPF deformation rates. Red line outlines landslide extent. Background is 2 m resolution ArcticDEM. (For interpretation of the references to colour in this figure legend, the reader is referred to the web version of this article.)

caused by a seasonal altitude-dependent temperature gradient and several other processes (Wegmüller et al., 2021; Samsonov and Feng, 2023). In mountainous areas, it manifests as an altitude-dependent seasonal signal, further complicating the detection of landslide-induced deformation. Thus, individual DInSAR interferograms and LOS time series are suboptimal for detecting and monitoring landslides, especially in mountainous areas that experience seasonal freeze and thaw.

5.2. 2D time series

2D deformation time series and rates are computed from ascending and descending interferograms in simultaneous processing implemented in MSBAS software. By default, ascending and descending SAR data are assumed to be acquired at different times, so the resulting 2D time series have a combined temporal resolution. This problem, however, is numerically unstable, so the Tikhonov regularization of zero, first, or

second-order is used in the software (Samsonov and d'Oreye, 2012). Alternatively, it is possible to resample ascending and descending data to a similar temporal grid to achieve a numerically stable solution but at a reduced temporal resolution. Practically, both approaches are possible with MSBAS, and both usually produce very similar results. However, resampling ascending and descending data to a similar temporal grid must be done outside the MSBAS software. For this study, we applied the Tikhonov regularization of the first order.

The 2D decomposition is, however, an approximation that assumes that the north-south deformation component is negligibly small. Horizontal deformation is rarely precisely eastward. For example, in this study, many observed landslides move in predominantly east-west directions due to their spatial orientation. If sliding occurs approximately along the east-west direction, the 2D deformation time series adequately captures the deformation progress.

The previously mentioned seasonal signal observed in the 1D deformation time series manifests only in a vertical component of the 2D deformation time series (Figs. 3b, d). Since slow-moving deep-seated landslides often occur on gently dipping slopes (Dai et al., 2023) (e.g., approximately 6° for the studied landslide in the Northwest Territories), the horizontal deformation component of these landslides is often larger than the vertical component. Thus, the east-west deformation component is the least noisy and captures landslide-induced deformation better. In this study, we mainly used the east-west deformation component for landslide characterization. Note that the sensitivity to horizontal deformation in DInSAR data is reduced with a decreasing SAR incidence angle.

5.3. Constrained 3D time series

All three deformation components cannot be reconstructed from space-borne ascending and descending data alone, except in the high Arctic (Gray, 2011) or if the landslide extent is large and the sliding rate is fast so that speckle offset tracking or multiple aperture interferometry techniques can be used (Strozzi et al., 2002; Bechor and Zebker, 2006). In some cases, however, all three deformation components can be reconstructed from space-borne ascending and descending data under the assumptions of the Surface-Parallel Flow (Joughin et al., 1998; Samsonov et al., 2020) or Aspect-Parallel Flow (Hu et al., 2018), or both, as in this study. With the MSBAS-3DSPF/3DAPF software, it is possible to compute the 3D deformation time series and then, from these time series, the resulting 3D deformation rates. Alternatively, the average 3D deformation rates can be calculated from the average LOS ascending and descending deformation rates. The latter approach is used here because it is less computationally intensive, and the deformation rate of the observed landslides during 2017–2022 remained nearly constant.

However, there are several issues with the constrained 3D approaches. In the case of 3DSPF, a numerical solution is not always possible due to the interplay between satellite geometries and the two (i.e., north and east) topographic gradients. In the case of 3DAPF, the numerical solution is undefined when the topography is flat. The areas where constrained 3D decompositions do not work can be removed based on the matrix condition number (Kang et al., 2023) computed by the MSBAS software for each pixel; however, it was not necessary in this study. The matrix condition number measures matrix sensitivity to errors in the input and is equal to the fraction of the maximal and minimal singular values.

It is a priori unknown if the constraint is valid in any specific case, e.g., if sliding occurs parallel to a uniform failure plane or in the direction determined by the slope aspect; thus, it is valuable to try both constraints. Assuming the validity of these constraints, the estimation of the sliding surface and direction depends on a filter strength applied to the DEM when computing topographic derivatives and the slope aspect. The filter strength is selected either manually through trial and error or in an automated adaptive way, depending on the distribution of the surface topography at a local scale (which may significantly vary from region to

region) and the landslide dimensions. Since the computation time of MSBAS-3DSPF/3DAPF applied to the LOS deformation rates is very short, various topographic gradients, produced with different filter strengths, can be tested for determining possible deformation scenarios. If a sliding surface cannot be accurately estimated in the case of 3DSPF or the sliding direction in the case of 3DAPF and validated by field observations, the MSBAS-2D technique is preferred to the constrained 3D techniques. In the current remote setting, field validation of the failure plane/sliding surface is complicated due to the necessity to drill through the frozen ground. In the case of the landslide in colluvium in the Northwest Territories, the failure plane may also be irregular, based on the results shown in Figs. 6(d, e) where there is an abrupt change in depletion and accumulation of material.

5.4. Landslide thickness

The 3D deformation rates can be used for computing the landslide thickness. However, the 3D SPF-constrained deformation rates are not a good substitute for the unconstrained 3D deformation rates. An assumption that the motion is parallel to the sliding plane also means that the vertical component reflects only the change in elevation due to sliding along the slope, and the methodology described by the eq. (2) cannot be applied because $\frac{\partial h}{\partial t} = 0$.

The 3D APF-constrained deformation rates do not require the motion to be parallel to the sliding plane, thus $\frac{\partial h}{\partial t} \neq 0$. But even in this case, to decompose deformation rates into sliding surface parallel and perpendicular components, we need to know the dip angle of the sliding surface, which, in general, is unknown. Only by assuming that the dip angle is constant for the entire plane the eq. (2) can be applied to vertical and horizontal deformation rates measured with DInSAR in the flat-earth reference system. Thus, this method accurately works only for the translation landslides that slide along the flat surface. In the previous studies, Booth et al. (2013) used vertical and horizontal velocities in the flat-earth reference frame (as in this study), while Hu et al. (2018) used the dip angle at the surface derived from DEM.

Several additional factors can impact landslide thickness calculations: 1) coefficient f describes the rheological properties of landslides in eq. (2) and 2) a regularization strength. Finally, in the computation, it was assumed that landslides have only one sliding surface. Based on the thickness distribution of the landslide in the Northwest Territories, it is possible to speculate that the central part of the landslide is affected by shallow deformation, in addition to sliding at a greater depth of approximately 100 m of the entire block. The maximum thickness of the landslide, which is 100 m, is close to the depth of permafrost in this area. Therefore, it can be speculated that the landslide is made of a frozen block that slides above unfrozen material. Furthermore, the sharp boundary in the northern part of the landslide body leads us to interpret that there may have been previous deformation processes that are presently unknown. However, without proper ground-based validation like in this study, the estimated landslide thickness should only be used as a low-precision estimate.

6. Conclusions

Using freely-available Sentinel-1 SAR data acquired during 2017–2022, we mapped two regions in northern Canada where several large slow-moving deep-seated landslides were observed. These landslides are located in remote areas, yet the impact of the landslides can be substantial. Several oil and gas wells and transportation corridors are located near some of the landslides in Alberta. It is, however, unknown if these wells are currently active. In both areas, landslides move towards moderate-size rivers that can be blocked in the case of landslide failure.

Among several time series techniques demonstrated here, 2D decomposition, implemented in the MSBAS-2D method, offers many benefits as it is very robust. The east-west deformation component is

most sensitive to the landslide motion occurring along gently dipping slopes, which was previously observed in another remote area in northeastern British Columbia, Canada (Samsonov and Blais-Stevens, 2023). It, however, cannot detect landslides moving along a north-south direction due to the lack of sensitivity of DInSAR to the motion in this direction. The vertical component is strongly affected by the seasonal altitude-dependent noise (Samsonov and Feng, 2023), which, at this time, cannot be fully corrected but can be reduced by applying spatial high-pass filtering. The constrained 3D decompositions can offer additional information about landslide motion, but they require an accurate estimation of the sliding plane and/or sliding direction, which is not always possible to estimate from DEM data alone. Due to the large extent and slow motion, GNSS and several other ground instruments can be deployed to improve our understanding of the dynamics of these landslides, making these landslides natural laboratories in permafrost areas. Thus, long-term DInSAR deformation (2017–2022) detected with Sentinel-1 imagery has helped us document very slow, large landslide movement in fine-grained sedimentary rocks contained within continuous to discontinuous permafrost settings of northern Canada.

Credit author statement

Samsonov conceptualized the study, processed satellite data and prepared figures. Blais-Stevens prepared physiographic settings. Both authors wrote the manuscript.

CRediT authorship contribution statement

Sergey V. Samsonov: Conceptualization, Data curation, Formal analysis, Funding acquisition, Investigation, Methodology, Project administration, Resources, Software, Supervision, Visualization, Writing – original draft, Writing – review & editing. **Andrée Blais-Stevens:** Funding acquisition, Validation, Writing – review & editing.

Declaration of competing interest

The authors have no competing interests to declare that are relevant to the content of this article.

Data availability

Sentinel-1 Synthetic Aperture Radar data in Single Look Complex format was downloaded from the Alaska Satellite Facility (<https://search.asf.alaska.edu>). The commercial GAMMA software was provided by Gamma Remote Sensing (<https://www.gamma-rs.ch>). Deformation products will be submitted to the Mendeley data repository upon paper acceptance.

Acknowledgment

We thank the European Space Agency for acquiring, and the National Aeronautics and Space Administration and Alaska Satellite Facility for distributing Sentinel-1 SAR data. ASTER-derived DEM and ArcticDEM were used in this study. Figures were plotted with GMT 6.0.0 and GnuPlot 5.2 software. The work was supported by the Canada Centre for Remote Sensing, NRCan, under the Earth Observation for Cumulative Effects, Phase 2 project and by the Geological Survey of Canada's Public Safety Geoscience program under the Office of Energy Research and Development Pipeline Geohazards project (GSC-19-103). NRCan contribution number/Numéro de contribution de RNCan: 20230138. Ariane Castagner helped with the literature review. The authors thank George Choma of the Canada Centre for Remote Sensing, NRCan, for help with proofreading. Supplementary data can be downloaded from <https://doi.org/10.17632/kc77435dkb.1>.

References

- Aylsworth, J., Duk-Rodkin, A., Robertson, T., Traynor, J., 2000. The physical environment of the Mackenzie Valley, Northwest Territories: a base line for the assessment of environmental change. Geological Survey of Canada. In: Bulletin 547. chapter Landslides of the Mackenzie Valley and Adjacent Mountainous and Coastal Regions, pp. 167–176. <https://doi.org/10.4095/211927>.
- Bechor, N., Zebker, H., 2006. Measuring two-dimensional movements using a single InSAR pair. *Geophys. Res. Lett.* 33 <https://doi.org/10.1029/2006GL026883>.
- Berardino, P., Fornaro, G., Lanari, R., 2002. A new algorithm for surface deformation monitoring based on small baseline differential SAR interferograms. *IEEE Trans. Geosci. Remote Sens.* 40, 2375–2383. <https://doi.org/10.1109/TGRS.2002.803792>.
- Booth, M.A., Lamb, M.P., Avouac, J.P., Delacourt, C., 2013. Landslide velocity, thickness, and rheology from remote sensing: La Clapière landslide, France. *Geophys. Res. Lett.* 40, 4299–4304. <https://doi.org/10.1002/grl.50828>.
- Casagli, N., Intrieri, E., Tofani, V., Gigli, G., Raspini, F., 2023. Landslide detection, monitoring and prediction with remote-sensing techniques. *Nature Reviews Earth & Environment* 4, 51–64. <https://doi.org/10.1038/s43017-022-00373-x>.
- Côté, M., Duchesne, C., Wright, J., Ednie, M., 2013. Digital compilation of the surficial sediments of the Mackenzie Valley corridor, Yukon coastal plain, and the Tuktoyaktuk peninsula. In: Technical Report. Geological Survey of Canada, Open File 7289. <https://doi.org/10.4095/292494>.
- Dai, X., Schneider-Muntau, B., Krenn, J., Zangerl, C., Fellin, W., 2023. Mechanisms for the formation of an exceptionally gently inclined basal shear zone of a landslide in glacial sediments - the Ludoialm case study. *Appl. Sci.* 13, 6837. <https://doi.org/10.3390/app13116837>.
- DeLuca, C., Zinno, I., Manunta, M., Lanari, R., Casu, F., 2017. Large areas surface deformation analysis through a cloud computing p-SBAS approach for massive processing of DInSAR time series. *Remote Sens. Environ.* 202, 3–17. <https://doi.org/10.1016/j.rse.2017.05.022>.
- Dille, A., Dewitte, O., Handwerger, A.L., d'Oreye, N., Derauw, D., Bamulezi, G.G., Mawe, G.I., Michellier, C., Moeyersoons, J., Monsieurs, E., Bibentyo, T.M., Samsonov, S., Smets, B., Kervyn, M., Kervyn, F., 2022. Acceleration of a large deep-seated tropical landslide due to urbanization feedbacks. *Nat. Geosci.* 15, 1048–1055. <https://doi.org/10.1038/s41561-022-01073-3>.
- Dudley, J.P., Samsonov, S.V., 2020. The Government of Canada automated processing system for change detection and ground deformation analysis from RADARSAT-2 and RADARSAT constellation Mission synthetic aperture radar data: description and user guide. In: Technical Report. Geomatics Canada Open File 63. <https://doi.org/10.4095/327790>.
- Duk-Rodkin, A., 1992. Surficial geology, Fort McPherson-Bell River, Yukon-Northwest Territories. Technical Report. Geological Survey of Canada, A Series Map 1745A. <https://doi.org/10.4095/184002>.
- Duk-Rodkin, A., Hughes, O.L., 1994. Tertiary-quaternary drainage of the pre-glacial Mackenzie basin. *Quat. Int.* 22–23, 221–241. [https://doi.org/10.1016/1040-6182\(94\)90015-9](https://doi.org/10.1016/1040-6182(94)90015-9).
- Fenton, M., Pawlowicz, J., Paulen, R., Prior, G., Olson, R., 2003. Quaternary geology of northern Alberta: Implications for kimberlite exploration. In: Conference: VII International Kimberlite Conference, Victoria, Canada, p. 5.
- Fuhrmann, T., Garthwaite, M., 2019. Resolving three-dimensional surface motion with InSAR: constraints from multi-geometry data fusion. *Remote Sens. (Basel)* 11, 241. <https://doi.org/10.3390/rs11030241>.
- Gray, L., 2011. Using multiple RADARSAT InSAR pairs to estimate a full three-dimensional solution for glacial ice movement. *Geophys. Res. Lett.* 38 <https://doi.org/10.1029/2010GL046484>.
- Green, R., Mellon, G., Carrigy, M., 1970. *Bedrock Geology of Northern Alberta, NTS 84 and NTS 74D, 74E, 74L and 74M*. Alberta Energy and Utilities Board, Alberta Geological Survey.
- Heginbottom, J., Dubreuil, M.A., Harker, P., 1995. Permafrost - Canada. (National Atlas of Canada MCR 4177, scale 1:7,500,000). Energy, mines, and resources Canada.
- Hu, J., Li, Z., Ding, X., Zhu, J., Zhang, L., Sun, Q., 2014. Resolving three-dimensional surface displacements from InSAR measurements: a review. *Earth Sci. Rev.* 133, 1–17. <https://doi.org/10.1016/j.earscirev.2014.02.005>.
- Hu, X., Lu, Z., Pierson, T., Kramer, R., George, D., 2018. Combining InSAR and GPS to determine transient movement and thickness of a seasonally active low-gradient translational landslide. *Geophys. Res. Lett.* 45, 1453–1462. <https://doi.org/10.1002/2017GL076623>.
- Hu, X., Burgmann, R., Schulz, W.H., Fielding, E.J., 2020. Four-dimensional surface motions of the Slumgullion landslide and quantification of hydro-meteorological forcing. *Nat. Commun.* 11 <https://doi.org/10.1038/s41467-020-16617-7>.
- Joughin, I., Kwok, R., Fahnestock, M., 1998. Interferometric estimation of three-dimensional ice-flow using ascending and descending passes. *IEEE Trans. Geosci. Remote Sens.* 36, 25–37. <https://doi.org/10.1109/36.655315>.
- Kang, Y., Lu, Z., Zhao, C., Qu, W., 2023. Inferring slip-surface geometry and volume of creeping landslides based on InSAR: a case study in Jinsha River basin. *Remote Sens. Environ.* 294, 113620 <https://doi.org/10.1016/j.rse.2023.113620>.
- Lane, L., Dietrich, J., 1996. Structural trends and bedrock geology in the Beaufort-Mackenzie region. In: Technical Report. Geological Survey of Canada, Miscellaneous Report, 59. <https://doi.org/10.4095/207661>.
- Li, L., Wen, B., Yao, X., Zhou, Z., Zhu, Y., 2023. InSAR-based method for monitoring the long-time evolutions and spatial-temporal distributions of unstable slopes with the impact of water-level fluctuation: a case study in the Xiluodu reservoir. *Remote Sens. Environ.* 295, 113686 <https://doi.org/10.1016/j.rse.2023.113686>.
- Liu, P., Li, Z., Hoey, T., Kincaid, C., Zhang, J., Zeng, Q., Muller, J.P., 2013. Using advanced InSAR time series techniques to monitor landslide movements in Badong of the three

- gorges region, China. *Int. J. Appl. Earth Obs. Geoinf.* 21, 253–264. <https://doi.org/10.1016/j.jag.2011.10.010>.
- Massonnet, D., Feigl, K., 1998. Radar interferometry and its application to changes in the Earth's surface. *Rev. Geophys.* 36, 441–500. <https://doi.org/10.1029/97RG03139>.
- Mougeot, C., Fenton, M., 2010. *Surficial Geology of the Whitesand River Area, Alberta (NTS 840)*. Energy Resources Conservation Board, ERCB/AGS Map, 541.
- Osmanoglu, B., Sunar, F., Wdowinski, S., Cabral-Cano, E., 2016. Time series analysis of InSAR data: methods and trends. *ISPRS J. Photogramm. Remote Sens.* 115, 90–102. <https://doi.org/10.1016/j.isprsjprs.2015.10.003>.
- Pawley, S., Hartman, G., Chao, D., 2016. Relative landslide susceptibility model of the Alberta Plains and shield regions (gridded data, geotiff format). In: Alberta Energy Regulator, AER/AGS Digital Data 2016-0044. URL: <https://ags.aer.ca/publication/dig-2016-0044>.
- Raspini, F., Bianchini, S., Ciampalini, A., Soldato, M.D., Solari, L., Novali, F., Conte, S.D., Rucci, A., Ferretti, A., Casagli, N., 2018. Continuous, semi-automatic monitoring of ground deformation using Sentinel-1 satellites. *Sci. Rep.* 8 <https://doi.org/10.1038/s41598-018-25369-w>.
- Samsonov, S., Blais-Stevens, A., 2023. Satellite interferometry for regional assessment of landslide hazard to pipelines in northeastern British Columbia, Canada. *Int. J. Appl. Earth Obs. Geoinf.* 118, 103273 <https://doi.org/10.1016/j.jag.2023.103273>.
- Samsonov, S.V., Feng, W., 2023. Deformation retrievals for North America and Eurasia from Sentinel-1 DInSAR big data approach, processing methodology and challenges. *Can. J. Remote. Sens.* 49 <https://doi.org/10.1080/07038992.2023.2247095>.
- Samsonov, S., Oreye, N., 2012. Multidimensional time series analysis of ground deformation from multiple InSAR data sets applied to Virunga Volcanic Province. *Geophys. J. Int.* 191, 1095–1108. <https://doi.org/10.1111/j.1365-246X.2012.05669.x>.
- Samsonov, S., Dille, A., Dewitte, O., Kervyn, F., Oreye, N., 2020. Satellite interferometry for mapping surface deformation time series in one, two and three dimensions: a new method illustrated on a slow-moving landslide. *Eng. Geol.* 266, 105471 <https://doi.org/10.1016/j.enggeo.2019.105471>.
- Samsonov, S., Tiampo, K., Cassotto, R., 2021. SAR-derived flow velocity and its link to glacier surface elevation change and mass balance. *Remote Sens. Environ.* 258, 112343 <https://doi.org/10.1016/j.rse.2021.112343>.
- Shi, X., Zhang, L., Zhou, C., Li, M., Liao, M., 2018. Retrieval of time series three-dimensional landslide surface displacements from multi-angularSAR observations. *Landslides* 15, 1015–1027. <https://doi.org/10.1007/s10346-018-0975-3>.
- Smittarello, D., d'Oreye, N., Jaspard, M., Derauw, D., Samsonov, S., 2022. Pair selection optimization for InSAR time series processing. *J. Geophys. Res. Solid Earth* 127. <https://doi.org/10.1029/2021jb022825>.
- Strozzi, T., Luckman, A., Murray, T., Wegmüller, U., Werner, C.L., 2002. Glacier motion estimation using SAR offset-tracking procedures. *IEEE Trans. Geosci. Remote Sens.* 40, 2384–2391. <https://doi.org/10.1109/TGRS.2002.805079>.
- Strozzi, T., Klimeš, J., Frey, H., Caduff, R., Huggel, C., Wegmüller, U., Rapre, A.C., 2018. Satellite SAR interferometry for the improved assessment of the state of activity of landslides: a case study from the cordilleras of Peru. *Remote Sens. Environ.* 217, 111–125. <https://doi.org/10.1016/j.rse.2018.08.014>.
- Wegmüller, U., Werner, C., 1997. GAMMA SAR processor and interferometry software. In: The 3rd ERS Symposium on Space at the Service of our Environment, Florence, Italy, pp. 1687–1692.
- Wegmüller, U., Magnard, C., Werner, C., Strozzi, T., Caduff, R., Manconi, A., 2021. Methods to avoid being affected by non-zero closure phase in InSAR time series analysis in a multi-reference stack. *Procedia Computer Science* 181, 511–518. <https://doi.org/10.1016/j.procs.2021.01.197>.
- Zebker, H., Villasenor, J., 1992. Decorrelation in interferometric radar echoes. *IEEE Trans. Geosci. Remote Sens.* 30, 950–959. <https://doi.org/10.1109/36.175330>.
- Zheng, W., Hu, J., Lu, Z., Hu, X., Sun, Q., Liu, J., Zhu, J., Li, Z., 2023. Enhanced kinematic inversion of 3-d displacements, geometry, and hydraulic properties of a north-south slow-moving landslide in three gorges reservoir. *J. Geophys. Res. Solid Earth* 128. <https://doi.org/10.1029/2022jb026232>.